Microsystem Technologies (2022) 28:1389–1397
https://doi.org/10.1007/s00542-019-04404-4

TECHNICAL PAPER

Development of energy harvesting MEMS vibration device sensor with wideband response function in low-frequency domain

Lan Zhang[1] · Ryohei Takei[1] · Jian Lu[1] · Natsumi Makimoto[1] · Toshihiro Itoh[1,2] · Takeshi Kobayashi[1]

Received: 31 August 2017 / Accepted: 15 March 2019 / Published online: 21 March 2019

Abstract
An aluminum-nitride (AlN) based microelectromechanical system (MEMS) vibration device sensor with a power-harvesting function is developed. We aimed at realizing a vibration sensor with wideband response in a low-frequency vibration domain, owing to the high-power density of vibration sources energy normally in a particular low frequency with several hertz deviations. A special design was implemented in this work, for the first time, to realize the sensor structure with a wideband response function. The given sensor has a disk-shaped proof mass attached to three sandwiched AlN spring flexures and a supporting beam system. Using MEMS techniques, the sensors were fabricated with the single die size of 7 × 7 mm and observed via scanning electron microscopy comprehensively. The functional feature of the electrical performance of the sensors was evaluated. The results demonstrated that with the given sensor, which has a low center resonant frequency of 57.5 Hz with a response feature of a half-voltage bandwidth of > 10 Hz, an output voltage of 2.4–4 mV at an acceleration of 0.1–0.6 g can be typically achieved. The low-frequency vibration sensor with a wideband response function can be used for many industrial and civilian applications to eliminate the restrictions on power sources.

1 Introduction

The development of big data technologies in the Internet of Things will lead to an increase in use of sensors in portable electrical devices, automobiles and machines, even in social infrastructures. However, this raises an issue for researchers and engineers: how can power be provided to these sensors? The mechanical energy from vibration sources is accessible and pervasive around the measured targets themselves, as Fig. 1 shows; many vibration sources exist in the surrounding environment, especially in the low-frequency vibration domain, such as automobiles, human bodies, and factory equipment (Beeby et al. 2006; Khalid et al. 2015; Cornes Technologies 2017). If a sensor can be used to sense the target vibration and efficiently obtain the energy from the vibration source simultaneously, it can be used to realize a real green sensing system by eliminating the power supply limitation.

The piezoelectric gauge method is a very useful technique for vibration devices; as a piezoelectric gauge experiences pressure or undergoes deformation, its electric charge will change. Under such a condition, vibration induces strain in the flexure and outputs electric charge to an external loading unit. Similar to the piezoresistive gauge principle (Kanda 1991; Peiner et al. 2006), the piezoelectric effect of semiconductor materials can provide a direct and convenient energy source for signal conversion between electrical and mechanical information. Thus, since piezoelectricity was demonstrated in 1880 by French physicists Jacques and Pierre Curie, the continued development of the piezoelectric technique has led to a huge market of products ranging from those for everyday use to more specialized devices. In the industry field, the piezoelectric gauge effect has been developed into a widely used application (Akiyama et al. 2006; Moubarak et al. 2011), such as pressure monitoring, acceleration measurement, temperature recording, and strain testing.

Many materials, both natural and synthetic, exhibit piezoelectricity such as AlN (Miwa and Fukumoto 1993; Dubois and Muralt 1999), lead zirconate titanate (PZT) (Du et al. 1998; Randall et al. 1998), quartz (Tajima et al.

✉ Lan Zhang
chou-ran@aist.go.jp

[1] Research Center for Ubiquitous MEMS and Micro Engineering (UMEMSME), National Institute of Advanced Industrial Science and Technology (AIST), Namiki 1-2-1, Tsukuba, Ibaraki 305-8564, Japan

[2] Graduate School of Frontier Sciences, The University of Tokyo, Kashiwanoha 5-1-5, Kashiwa, Chiba 277-8563, Japan

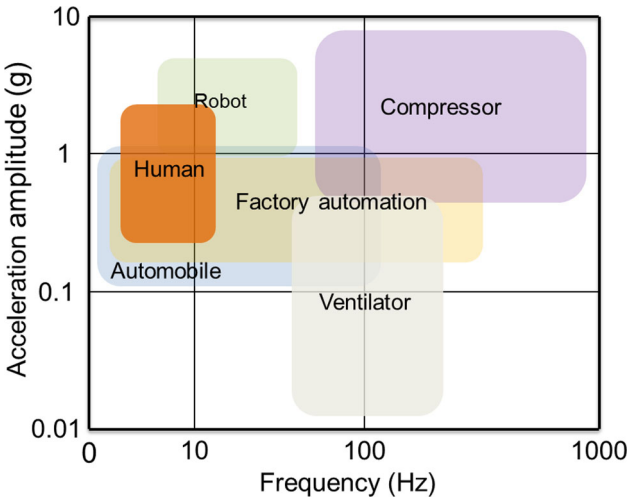

Fig. 1 Vibration sources in the surrounding environment

1998), lanthanum gallium silicate (Shimamura et al. 1996), gallium orthophosphate (Krempl et al. 1997), and lithium niobate (Smith and Welsh 1971). Among the piezoelectric materials, AlN has a very good cost performance. AlN has a controllable fabrication cost with a reasonable energy density and is environment friendly. Although AlN materials can only generate a limited output power, a thin film AlN-based cantilever micro-generator with a center resonant frequency of 1368 Hz was developed, which can generate 2 μW @ 4-g acceleration amplitude (Marzencki et al. 2008). An AlN harvester has also been developed, which can generate a DC power of 0.514 μW @ 2.49 V, under an applied vibration with an acceleration amplitude of 0.05 g at a center frequency of 46.6 Hz (Takei et al. 2016, 2017).

Several years ago, Liu et al. (2011, 2014) developed a low-frequency piezoelectric vibration harvester by arraying the parallelly arranged cantilever elements; the sensors had a wide band, and steadily increased the power generation from 19.4 to 51.3 nW within the operating frequency bandwidth, ranging from 30 to 47 Hz at 1.0 g. Moreover, recently, some researchers (Yaghootkar et al. 2017) developed a wideband high-frequency piezoelectric vibration sensor with an energy harvesting function. Table 1 shows the comparison between the MEMS-wideband vibration sensors with power harvesting function. It is clear that energy-harvesting MEMS vibration devices are a very charming research area for MEMS researchers and engineers, particularly the fabrication of an energy harvesting MEMS sensor with a wideband response function in the low-frequency domain. In a previous work (Zhang et al. 2016), we developed an s-shaped spring sensor, which can be used to sense a specific low-frequency vibration and implement energy harvesting in a narrowband domain. The mechanical properties of the device structure, including the resonant frequency, initial deformation, and vibration modes, were theoretically and experimentally investigated to validate the vibration sensor design. The functional performance of the vibration output under different amplitudes was also comprehensively evaluated. However, vibration sources in the surrounding environment do not converge at a specific frequency, owing to the high-power density of their vibration energy in a particular low-frequency domain with several hertz of deviations. If the vibration sensor has a resonance frequency with a wideband response range, it can sense and convert low-frequency vibration sources' power into electricity efficiently and in large amounts. Thus, the purpose of this work is to develop a wideband vibration sensor with an energy-harvesting function for sensing low-frequency vibrations.

We designed herein a special structure of the vibration sensor with a wideband response function in a low-frequency domain. We fabricated the given sensor with different flexure sizes by using a micromechanical technique. The measurement results of the X-ray diffractometer (XRD) spectra and the wafer curvatures were used to evaluate the film properties of the AlN-piezoelectric layer. We observed the micro-structure of the fabricated energy-harvesting sensor using scanning electron microscopy (SEM). A comparison of the voltage output features with different supporting-beam widths was made. The performance of the voltage output of the fabricated sensor with different vibration amplitudes was measured and compared comprehensively.

Table 1 MEMS-wideband vibration sensors with power harvesting function

	Resonant frequency (Hz)	Bandwidth (Hz)	Output power/voltage	Features
Li et al. (2015)	12	> 2	4.5 mW@1 g	Multiple cantilever
Liu et al. (2011)	36	17	51.3 nW@1 g	Multiple PZT elements
Guilllemet et al. (2013)	150	> 10	2.2 μW@1 g	Interdigitated combs
Liu et al. (2014)	383.7	> 100 (nonlinear)	0.339 mV@1 g	Hybrid frequency broadening
Yaghootkar et al. (2017)	12 k	> 500	350 mV@1 g	Diaphragm

2 Design and fabrication of wideband vibration sensor

2.1 Design of vibration sensor

We developed a novel type of vibration sensor with a wideband response function, which has an energy harvesting function in a low-frequency domain with a wideband response range (around 10 Hz). The given harvester will be used for measuring external vibrations or inertial acceleration perpendicular to the device sensor. Figure 2 shows a schematic of the wideband low-frequency vibration device with typical structures, which has a top surface composed of micro-machined sandwiched AlN-piezoelectric gauges. The sensor flexures are much thinner than the proof mass, i.e., only the springs bend during vibration. Similar to its sister type (Zhang et al. 2016), the proposed sensor has a large proof mass attached to a triple sandwiched spring-flexure system. The typical sensor has a cylinder-shaped proof mass (diameter: 2.5 mm; thickness: 400 µm). The difference is that every series(S) spring–flexure unit attaches to the supporting beams to realize a sensor with a power-harvesting function in a wideband frequency response domain. Moreover, the piezoelectric material of the PZT was replaced with AlN, because AlN has the advantages of a uniform microstructure and excellent resistance to thermal shock (Bardaweel et al. 2006). The excellent performance of AlN materials as regards resistance to thermal shock enables the piezoelectric gauge to enjoy a high-stability performance for complicated application conditions (e.g., in a factory or a field site, where the working temperature frequently varies).

2.2 Fabrication process and apparatus

Six photo masks are used to fabricate the device sensor by micromachining. Figure 3 shows the fabrication sequence of given wideband vibration energy-harvesting sensor. The MEMS process starts from a silicon-on-insulator (SOI) wafer substrate with a thickness and diameter of 400 µm and 100 mm, respectively. The SOI wafer has a 1-µm-thick box layer under a 5-µm-thick active Si layer (see Fig. 3a). After initial cleaning by immersing the wafer in a piranha solution at 100 °C for 10 min, a 1.55-µm-thick thermal oxide layer is grown on the top surface of the active Si layer (see Fig. 3b). Simultaneously, active layer of Si with sub-micrometer thickness was used to generate a thermal oxide layer. Using the sputtering processes, sandwiched layers of 85-nm platinum (Pt)/15-nm titanium (Ti), 1.5-µm AlN, and 100-nm Pt/8-nm Ti were generated on the surface of the SOI wafer (see Fig. 3c). Photolithography and ion-milling were used to pattern and dry-etch the upper electrode, piezoelectric, and bottom electrode layers with high precision (see Fig. 3d). Then, to fabricate the spring-flexure structures, the active Si layer was etched via inductively coupled plasma reactive-ion etching (ICP) and the SiO_2 box layer was etched via reactive ion etching (RIE) (see Fig. 3e). Finally, the proof mass was released from the back of the wafer by ICP, and O_2 plasma was used to remove the fluorine resin and other residuals (see Fig. 3f).

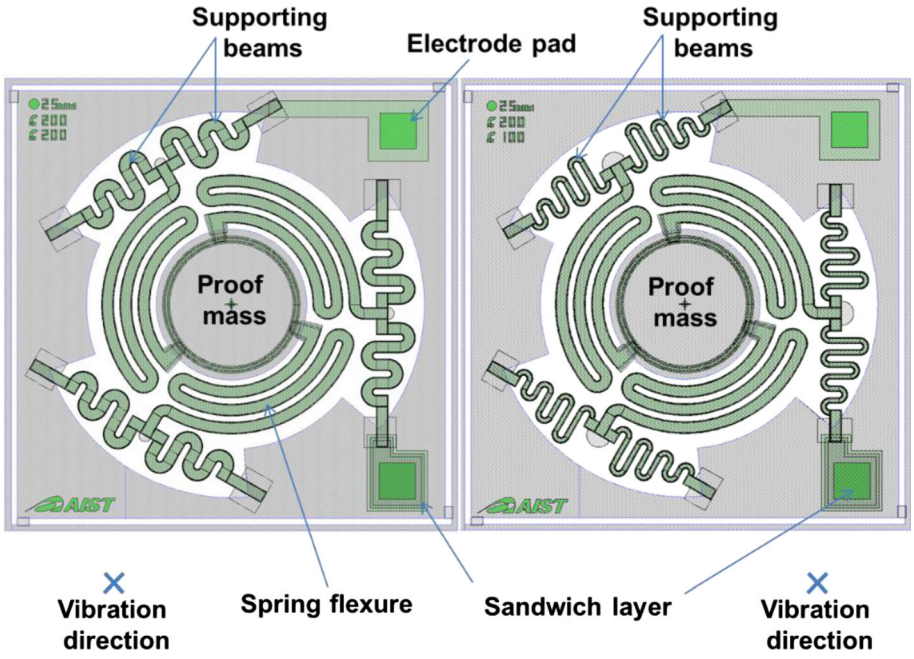

Fig. 2 Typical layout of the wideband low-frequency vibration sensor structures

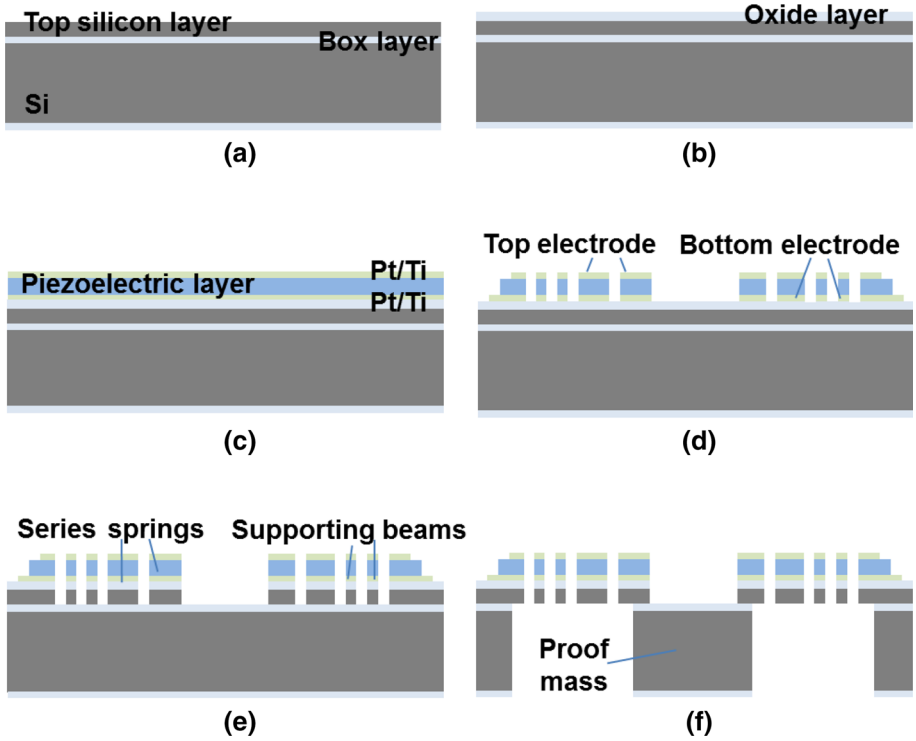

Fig. 3 Fabrication sequence. **a** SOI wafer preparation. **b** Oxide layer generation. **c** Metallic electrode and AlN-piezoelectric layer deposition. **d** Metallic electrode and piezoelectric layer etching. **e** Flexure structures etching. **f** Proof mass release and cleaning

Several micromachine apparatuses were used to fabricate the MEMS vibration sensor. The top–bottom electrodes and the piezoelectric layer were generated using sputter deposition equipment (SME-200E, ULVAC Technologies, Inc.). Ion-milling (M-8038, NS Co., Ltd.) was used to etch the electrode metal and the AlN layers with the desired patterns. The ICP etching equipment (MUC-21, SPP Technologies Co., Ltd.) was used to etch the SOI wafer on the top and back sides, and release the sensor mass proof to be a movable structure. Meanwhile, the RIE apparatus (RIE-10NRS SAMCO Co., Ltd.) was used to etch the silicon dioxide in the passivation and box layers.

2.3 Measurement system and equipment

Figure 4 shows a flow chart of the operating measurement system. Sweep signals were generated by a computer-controller unit. Control signals were then transmitted to the amplifier by a digital-to-analog converter. The actuation signal drove the shaker, generating vibrations, set in a vertical direction with respect to the vibration sensor springs at different frequencies. The given sensor was placed on the shaker to detect vibrations and controller implant the acquisition of output signal from the vibration sensor with an analog-to-digital converter.

An X-ray diffractometer (XRD) (D8 Discover Hybrid/S, Bruker Co., Ltd.) was used to scan the AlN-wafer surface and characterize the AlN-piezoelectric layer on the target wafer. SEM (S-3000H, Hitachi Co., Ltd.) was used to observe the structure of the fabricated vibration sensor. A test system composed of a computer, a controller (Spider-81B, Crystal Instruments, Inc.), an amplifier (APS-125-100, APS Dynamics, Inc.), and a shaker (APS-113HF, APS Dynamics, Inc.) was designed to evaluate the performance of the fabricated vibration sensors. A desk-type anti-vibration table (HOA-129-100LA, Sigma Koki Co., Ltd.) was used to isolate the measurement system and ground environment and eliminate the effects of ambient noise.

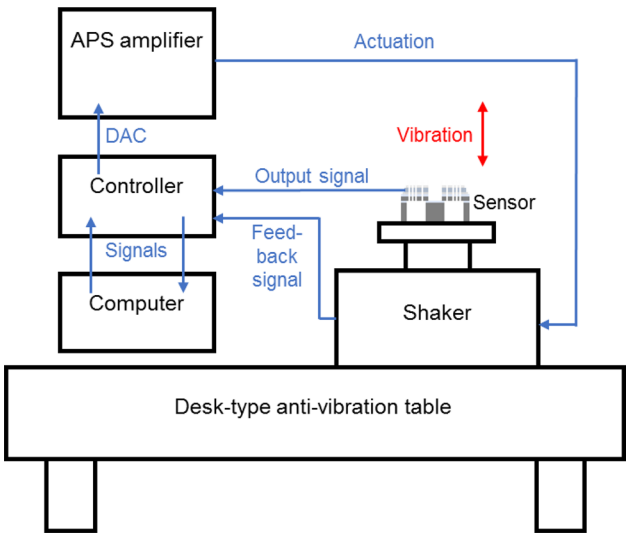

Fig. 4 Configuration and flow chart of the measurement operating system

3 Evaluation of fabricated sensor

3.1 XRD measurement of AlN wafer

XRD with radiation was performed to examine the crystalline quality and orientation of the piezoelectric layer. The XRD equipment was set with the scanning parameters of 50 kV and 100 mA and the scanning beam had a corresponding 300-μm diameter. Figure 5a–d shows a comparison of the XRD patterns of the AlN film on the Pt/Si wafer with different testing positions. These figures illustrate a high-intensity diffraction peak related to AlN at 36.0°. The full width at half maximum of the peak corresponding to AlN is approximately 0.4°. According to the Scherrer formula, the average crystal size of AlN films is 21.8 nm. The inset in Fig. 5a shows the testing positions on the Pt/Si wafer. The results show that different testing positions exhibited substantial uniformity in orientation with preferred intensity values from 2431 to 2985 (arb. units). The dispersion errors were within 18.5%. These results indicated that the sputtered AlN-piezoelectric film had a homogeneous surface, which was very suitable for use in developing an electronic device (Diao et al. 2014). The largest peak, marked at 40°, is associated with Pt (111) because of the strong orientation. The inset in Fig. 5b shows a typical optical image of the AlN/Pt/Si wafer. The high brightness light also can be used to check the cracks on the surface of the AlN film.

3.2 Measurement of the wafer curvatures caused by the piezoelectric film

The piezoelectric film structures in the MEMS fabrication process are generally prone to intrinsic stress on the target wafer and caused a curvature surface. Thus, the wafer curvatures caused by the piezoelectric film and other oxide/metal films must be understood. Figure 6 shows the measured wafer curvatures before the piezoelectric AlN film deposition, after the AlN film deposition, and the deflection value caused by AlN without stress balance layer coating. The sputtering cumber temperature for the AlN film generation was set at 365 °C. The thickness of the generated AlN was tested at 1.45 μm. As Fig. 6 shows, the maximum deflection across the wafer was 42.5 μm after oxide layer and bottom electrode layer deposition. The maximum wafer deflection across the wafer then became only − 1.07 μm when the AlN layer was generated. Moreover, the deflection value caused by the AlN film coating was an absolute value of − 43.64 μm. Less wafer bending can eliminate the piezoelectric film cracking, and the stress-caused cracking is unfavorable for the lithography and fabrication process (Lu et al. 2006).

3.3 SEM observation of fabricated sensors

Figure 7 shows the typical SEM images of the vibration sensor harvester structure and local magnifications. Figure 7a illustrates the overall structure of the typical sensor surrounded by a Si substrate. The sensor had a 2.5 mm-diameter and 400 μm-thick proof mass at the center and three units of a spring–flexure system surrounding it for support. Each unit had one 200 μm-wide and 7 μm-thick S-spring flexure with two 7 μm-thick supporting beams fixed at both ends. The supporting beams were used to fix the proof mass and the spring flexure to the surrounding silicon substrate.

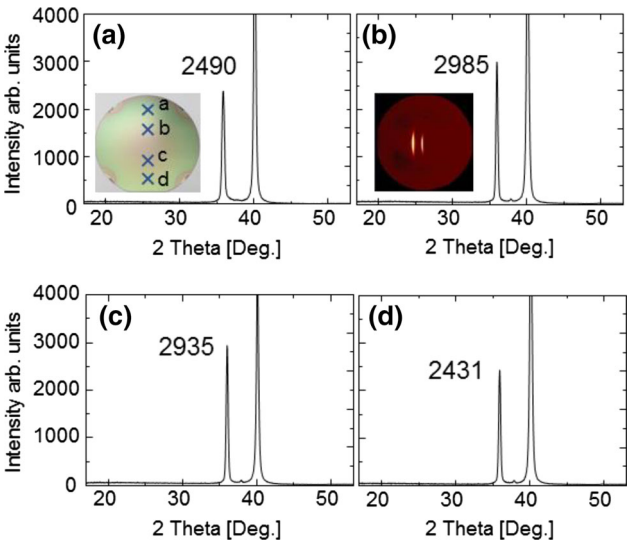

Fig. 5 XRD patterns of AlN-piezoelectric film on Pt/Si wafer

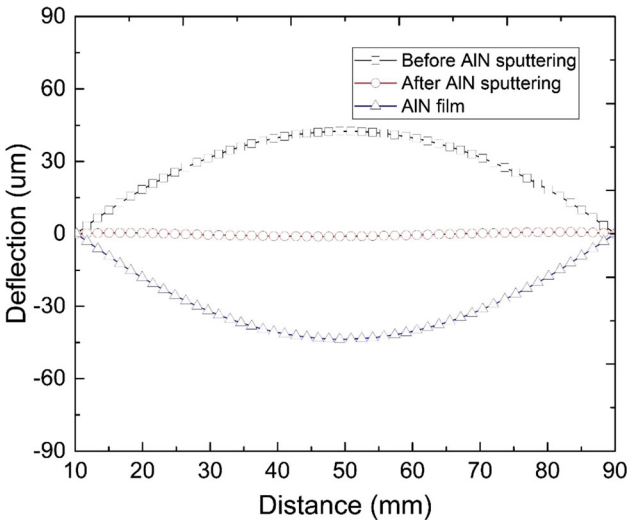

Fig. 6 Measured wafer curvatures before the piezoelectric AlN film deposition and after the AlN film deposition and the deflection value caused by AlN without stress balance layer coating

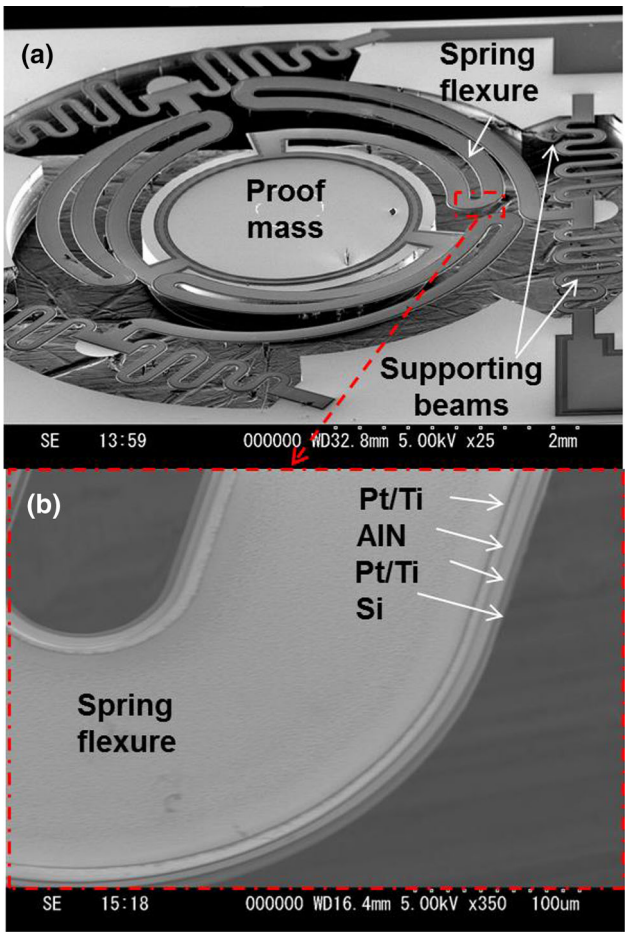

Fig. 7 **a** SEM image of the typical wideband low-frequency MEMS vibration device. **b** Magnified SEM image of the sandwiched AlN piezoelectric gauge structure

Figure 7b shows a magnified image of the sandwiched AlN-piezoelectric structure on the spring flexure. As shown, the microstructures of the sandwiched structures are successfully realized by the MEMS fabrication process with precision. The spring-system flexure structure was released completely, and the top electrode, piezoelectric layer, and bottom electrode were fabricated on it. The given sensor layout realizes a final device die size of less than 7 mm × 7 mm, which can greatly reduce its production cost.

3.4 Evaluation of wideband low-frequency vibration device

3.4.1 Comparison of the electrical output features with the supporting beam width

Two typical 200-μm S-spring flexure vibration devices were measured. They had 100-μm and 200-μm supporting beams. The vibration device sensors were subjected to a 0.1 g peak-to-peak sweeping signal of a sinusoidal wave from 40 to 70 Hz. Figure 8 shows the output voltage of the 2.5 mm-diameter proof mass vibration sensors with different supporting beams in a sweeping frequency domain. The results demonstrated that an output voltage of up to 2.4 mV at an acceleration of 0.1 g can be achieved. The controller integrated an ADC converter, which can convert the AC voltage of the sensors' output into an effective root mean square (RMS) DC value. The peak-to-peak (p–p) AC output voltage should be equal to $2\sqrt{2}$ times the RMS value (i.e., the sensors can generate a maximum p–p voltage of 6.8 mV under a 0.1 g amplitude vibration).

The comparison of the results from the two figures showed that the typical sensors with different supporting beams had a similar central resonance frequency at 57.5 Hz with a very small different value (i.e., approximately 0.2 Hz). Considering the structure of the given sensors, the supporting beams were fixed at both ends and used to support the spring flexures to the surrounding silicon substrate. The varying width of the supporting beam

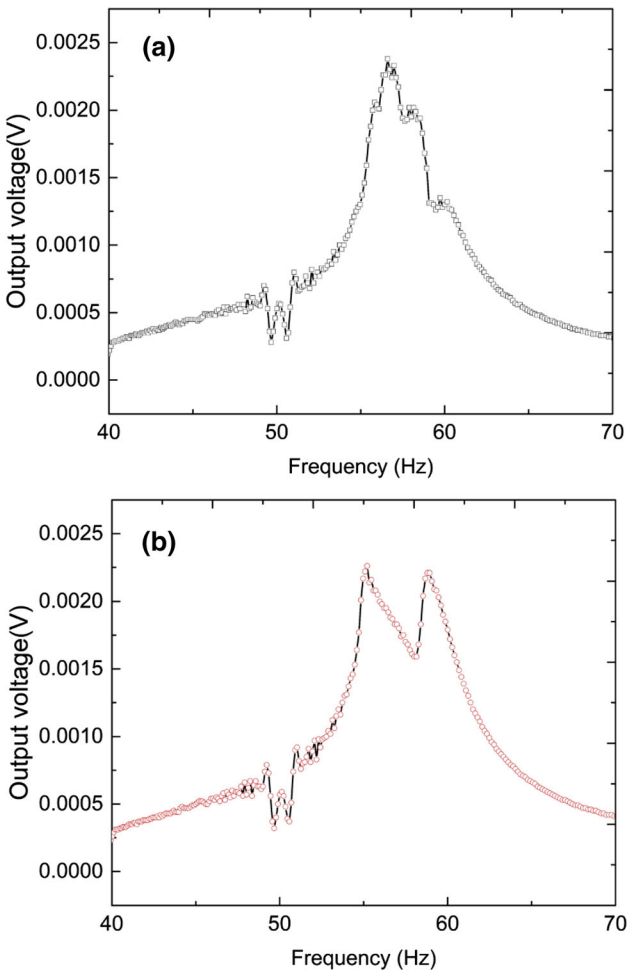

Fig. 8 Measured voltage output of the wideband vibration sensor with different supporting beams: **a** 200 μm and **b** 100 μm widths

may have mainly contributed to the effect of softening the device structure to extend the bandwidth, but only slightly changed the center resonance. Notably, a peak at approximately 50 Hz was found in both devices in Fig. 8, which was believed to be caused by the resonant frequency of the anti-vibration desk.

Based on the half-voltage output principle, the functional performance of the given sensors has been confirmed, i.e., the 200 μm supporting beam sensor has a 5-Hz effective bandwidth and the 100 μm supporting beam sensor has a 7-Hz effective bandwidth. The results show that the relative changes in the output bandwidth increase with decreasing width of the supporting beam, i.e., the effective bandwidth was extended by 2 Hz by narrowing the width of the supporting beam. Via comparison with the results of the sister-type narrowband vibration sensor (Zhang et al. 2016), the wideband response feature was realized and confirmed. The narrow supporting beam configuration can extend the bandwidth response of the vibration sensor; however, narrow beams can easily result in structural damage as a result of shock or large vibrations. Moreover, narrow beams may be difficult to package and unreliability due to the original deformation of the proof mass and the limitations of the manufacturing accuracy. Thus, the balance between the desired functional property and manufacturing yield should be considered in commercial fabrication.

3.4.2 Comparison of output voltage with different amplitudes

The functional feature of the electrical performance of the vibration device sensor was evaluated. A typical sensor with a 2.5-mm diameter mass proof with a 200-μm-wide S spring and 200-μm-wide supporting beams was used. Figure 9 shows the measured voltage output of the vibration device for acceleration values of 0.1 g to 0.6 g in a sweeping frequency domain. The wideband response function of the typical sensor has a central frequency at 57.5 Hz, and the output voltage with the wideband feature was confirmed. The results demonstrate that an RMS voltage output up to 4 mV at an acceleration of 0.6 g can be achieved.

Figure 10 shows the analysis result of a typical sensor's output bandwidth and peak voltage with different acceleration amplitudes. The half-voltage bandwidth increased from 5 to 15 Hz with increasing acceleration amplitude from 0.1 to 0.6 g. The reason for this could be that the different effective stiffnesses of the supporting beams and S-flexure springs causes incongruity in the vibration feature during the increase of the acceleration amplitude (Halim and Park 2015). A change in the vibration acceleration also changes the voltage output from 2.4 to 4 mV. Clearly, the vibration sensor had a largest output at the largest acceleration amplitude. The sensor output increased with an increase in the vibration acceleration. The sensor almost achieved a peak output value at an acceleration of 0.3 g; however, after that, the rate of increase of the output voltage was not proportional to that of the acceleration amplitude. The reason for this is that the vibration amplitude increase can cause an increase in the piezoelectric gauge deformation; however, nonlinear deformation on the flexure cannot cause the output of piezoelectric gauge to maintain a consistent change rate with the vibration amplitude. Some longer spring device sensors with bigger proof masses can be subjected to larger vibration amplitudes to partly improve the output voltage, and this can also partly be used to extend the consistent change rate between the output voltage and vibration amplitude in a larger range. However, the factors similar to those previously

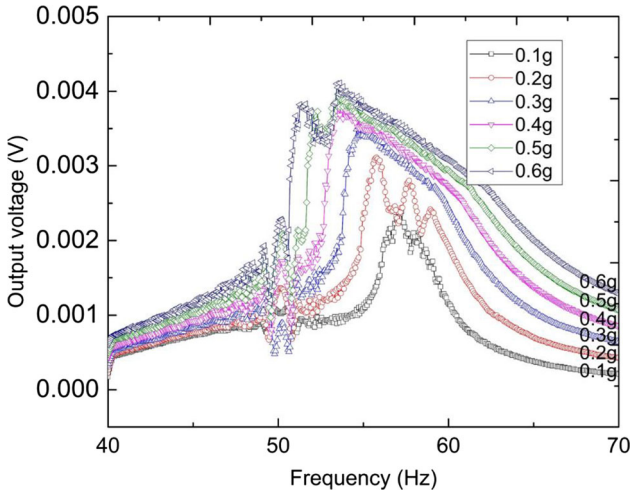

Fig. 9 Measured voltage output of typical vibration device with different acceleration amplitudes

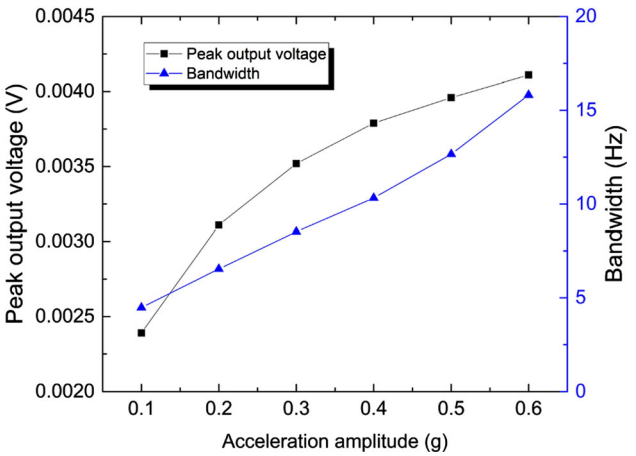

Fig. 10 Comparison of typical device output bandwidth and peak voltage with different acceleration amplitudes

mentioned, i.e., that the longer spring flexure configuration has a fragile structure and that a bigger proof mass suffers from a larger configuration should be considered in commercial fabrication.

3.4.3 Sensor power output

Finally, the power output of the typical sensor having a 2.5-mm-diameter mass proof and 200-μm-wide S spring flexures and supporting beams was studied. The wideband vibration device sensor can generate an output power up to 0.017 μW under a 0.5-g acceleration amplitude. The measured value is comparable to that of the first-generation vibration sensor of the Marzenki group (2005) and much lower than that of other sensors (Marzencki et al. 2008; Takei et al. 2017). The reasons for this could be as follows: (i) the absolute dimensions and piezoelectric gauge area of this wideband device sensor are much smaller than those of others. The sensor output can be improved by increasing the sensor dimensions and enlarging the piezoelectric gauge area. (ii) to ensure process stability and yield, in the first trial produce, the piezoelectric layer was deposited over the whole area of the spring flexures, and as a result, a part of the output power was offset by the piezoelectric effect on the fixed end of the spring flexures. By optimizing the piezoelectric layer pattern on the flexure, this issue can be overcome.

4 Conclusion and outlook

We presented herein a low-frequency MEMS vibration sensor with a wideband response feature. AlN was used as the piezoelectric gauge layer to realize the energy-harvesting function of the given sensor. A special design of the sensor structure with a disk-shaped proof mass attached to three sandwiched AlN spring flexures and supporting beam system was implemented for the first time.

The sensors were fabricated using micromachining processes, with a single die size of 7 × 7 mm. The energy-harvesting sensor was observed using SEM; in particular, the micro-machined structures are fabricated precisely and protected well during the fabrication process. The film properties of the AlN piezoelectric layer exhibited an ideal performance by analyzing the measurement results of the XRD spectra and the wafer curvatures. The functional feature of the electrical performance of the energy-harvesting sensor was evaluated. The results demonstrated that the given sensor has a low central resonant frequency of 57.5 Hz with a response feature of the half-voltage bandwidth > 10 Hz. An output voltage of 2.4–4 mV at acceleration range of 0.1–0.6 g can be typically achieved.

In order to harvest the power from the output voltage through the internal capacitor and resistor of piezoelectric material, synchronized switch harvesting on inductor (SSHI, Takei et al. 2016, 2017) and random mechanical switching harvesting on inductor (RMSHI, Giusa et al. 2013) methods are the most effective methods. Especially, the novel approach of RMSHI, which is very good at collecting and storing energy from weak random vibrations with zero voltage threshold. However, the given device has a several mV level voltage output only, which cannot able to generate enough output voltage larger than the diode threshold in the given circuits. Finally, the output voltage was which was evaluated by a very high sensitivity testing system; the main reason for this was that the piezoelectric layer was deposited on the entire spring structure. During the vibration, the piezoelectric effect of spring flexure on beam ends canceled each other's output voltages. The authors considered that the output voltage of wideband sensors should be modified in the next stage of fabrication. We will redesign the layout of piezoelectric gauge, i.e., pattern the AlN-layer on the stress area on the spring flexure only. This issue can be modified in a certain way. We hope that the low-frequency energy-harvesting sensor with a wideband response function can be used to realize many applications in civil and industrial fields.

Acknowledgements This work has been conducted as one of the research topics of the New Energy and Industrial Technology Development Organization (NEDO) project "Utility Core Monitoring System Development (UCoMS)."

References

Akiyama M, Morofuji Y, Kamohara T, Nishikubo K, Tsubai M, Fukuda O, Ueno N (2006) Flexible piezoelectric pressure sensors using oriented aluminum nitride thin films prepared on polyethylene terephthalate films. J Appl Phys 100:114318-1–114318-5

Bardaweel H, Al Hattamleh O, Richards R, Bahr D, Richards C (2006) A comparison of piezoelectric materials for MEMS power generation. In: The sixth international workshop on micro and nanotechnology for power generation and energy conversion applications, Nov. 29–Dec. 1, 2006, Berkeley, USA, pp 207–210

Beeby S, Tudor M, White N (2006) Energy harvesting vibration sources for microsystems applications. Meas Sci Technol 17:R175–R195

Cornes Technologies (2017) Vibration harvesting device development. https://www.cornestech.co.jp

Diao Y, Shaw L, Bao Z, Mannsfeld S (2014) Morphology control strategies for solution-processed organic semiconductor thin films. Energy Environ Sci 7:2145–2159

Du X, Zheng J, Belegundu U, Uchino K (1998) Crystal orientation dependence of piezoelectric properties of lead zirconate titanate near the morphotropic phase boundary. Appl Phys Lett 72:2421–2423

Dubois M, Muralt P (1999) Properties of aluminum nitride thin films for piezoelectric transducers and microwave filter applications. Appl Phys Lett 74:3032–3034

Giusa F, Giuffrida A, Trigona C, Andò B, Bulsara A, Baglio S (2013) "Random Mechanical Switching Harvesting on Inductor": a novel approach to collect and store energy from weak random vibrations with zero voltage threshold. Sens Actuators, A 198:35–45

Guilllemet R, Basset P, Galayko D, Cottone F, Marty F, Bourouina T (2013) Wideband MEMS electrostatic vibration energy harvesters based on gap-closing interdigited combs with a trapezoidal cross section. In: Proceedings of the IEEE MEMS 2013, pp 817–820

Halim M, Park J (2015) Piezoceramic based wideband energy harvester using impact-enhanced dynamic magnifier for low frequency vibration. Ceram Int 41:S702–S707

Kanda Y (1991) Piezoresistance effect of silicon. Sens Actuators A28:83–91

Khalid A, Kumar Redhewal A, Kumar M, Srivastav A (2015) Piezoelectric vibration harvesters based on vibrations of cantilevered bimorphs: a review. Mater Sci Appl 6:818–827

Krempl P, Schleinzer G, Wallnofer W (1997) Gallium phosphate, $GaPO_4$: a new piezoelectric crystal material for high-temperature sensorics. Sens Actuators, A 61:361–363

Li P, Liu Y, Wang Y, Luo C, Li G, Hu J, Liu W, Zhang W (2015) Low-frequency and wideband vibration energy harvester with flexible frame and interdigital structure. AIP Adv 5:047151-1-8

Liu H, Tay C, Quan C, Kobayashi T, Lee C (2011) Piezoelectric MEMS energy harvester for low-frequency vibrations with wideband operation range and steadily increased output power. J Microelectromech Syst 20:1131–1142

Liu H, Koh K, Lee C (2014) Ultra-wide frequency broadening mechanism for micro-scale electromagnetic energy harvester. Appl Phys Lett 104:053901-1–053901-3

Lu J, Kobayashi T, Zhang Y, Maeda R, Mihara T (2006) Wafer scale lead zirconate titanate film preparation by sol-gel method using stress balance layer. Thin Solid Films 515:1506–1510

Marzencki M, Basrour S, Charlot B, Grasso A, Colin M, Valbin L (2005) Design and fabrication of piezoelectric micro power generators for autonomous microsystems. In: Symposium on design, test, integration and packaging of MEMS/MOEMS (DTIP'05), June 1–3, 2005, Montreux, Switzerland, pp 299–302

Marzencki M, Ammar Y, Basrour S (2008) Integrated power harvesting system including a MEMS generator and a power management circuit. Sens Actuators, A 145–146:363–370

Miwa K, Fukumoto A (1993) First-principles calculation of the structural, electronic, and vibrational properties of gallium nitride and aluminum nitride. Phys Rev B 48:7897–7902

Moubarak P, Ben-Tzvi P, Zaghloul M (2011) A self-calibrating mathematical model for the direct piezoelectric effect of a new MEMS tilt sensor. IEEE Sens J 12:1033–1042

Peiner E, Tibrewala A, Bandorf R, Biehl S, Luthje H, Doering L (2006) Micro force sensor with piezoresistive amorphous carbon strain gauge. Sens Actuators, A 130–131:75–82

Randall C, Kim N, Kucera J, Cao W, Shrout T (1998) Intrinsic and extrinsic size effects in fine-grained morphotropic-phase-boundary lead zirconate titanate ceramics. J Am Ceram Soc 81:677–688

Shimamura K, Takeda H, Kohno T, Fukuda T (1996) Growth and characterization of lanthanum gallium silicate $La_3Ga_5SiO_{14}$ single crystals for piezoelectric applications. J Cryst Growth 163:388–392

Smith R, Welsh F (1971) Temperature dependence of the elastic, piezoelectric, and dielectric constants of lithium tantalate and lithium niobate. J Appl Phys 42:2219–2230

Tajima I, Asami O, Sugiura E (1998) Monitor of antibodies in human saliva using a piezoelectric quartz crystal biosensor. Anal Chim Acta 365:147–149

Takei R, Okada H, Makimoto N, Itoh T, Kobayashi T (2016) Simulation of an ultralow-power power management circuit for MEMS cantilever piezoelectric vibration energy harvesters. Jpn J Appl Phys 55:10TA06-1-5

Takei R, Okada H, Noda D, Ohta R, Takeshita T, Itoh T, Kobayashi T (2017) High-efficiency MOSFET bridge rectifier for AlN MEMS cantilever vibration energy harvester. Jpn J Appl Phys 56:04CC03-1-4

Yaghootkar B, Azimi S, Bahreyni B (2017) A high-performance piezoelectric vibration sensor. IEEE Sensors J 17:4005–4012

Zhang L, Lu J, Takei R, Makimoto N, Itoh T, Kobayashi T (2016) S-shape spring sensor: sensing specific low-frequency vibration by energy harvesting. Rev Sci Instrum 87:085005-1–085005-8